physica status solidi (a)

RESEARCH ARTICLE OPEN ACCESS

Optimization FTO/c-TiO_2 Capped with m-TiO_2 Electron Transport Layer for Efficient Interfacial Charge Carriers' Extraction and Transport Prepared by Spray Pyrolysis

Sizwe Sibiya | Mmantsae Diale

Department of Physics, University of Pretoria, Pretoria, South Africa

Correspondence: Mmantsae Diale (mmantsae.diale@up.ca.za)

Received: 12 June 2025 | **Revised:** 6 October 2025 | **Accepted:** 20 October 2025

Keywords: charge carriers' mobility | perovskite | spray pyrolysis | titanium dioxide | trap states

ABSTRACT

This study explores the fabrication of compact-titanium dioxide (c-TiO_2) electron transport layer capped with mesoporous-titanium dioxide (m-TiO_2) using spray pyrolysis while controlling layer thickness. X-ray diffraction confirmed a crystalline rutile c-TiO_2 structure, with crystallite size increasing from 22 to 24 nm as deposition time increased. Field emission-scanning electron microscopy showed uniform surface coverage, with average grain size increasing from 195.57 to 242.34 nm, and UV–vis spectra indicated a bandgap near 430 nm. Electrical measurements revealed improved conductivity (3×10^6 to 1.18×10^7 S/m) and reduced sheet resistance (7.34–6.33 Ω/□). The best conductivity was achieved with a 7 s *meso*-epitaxial TiO_2 layer, enhancing electron transport and charge carrier mobility. Current-voltage (I–V) characteristics demonstrated enhanced electron transport properties, with increased charge carrier mobility from 1.059×10^3 to 2.523×10^3 $cm^2V^{-1}s^{-1}$. Furthermore, electron-only devices with *meso*-passivated TiO_2 showed a higher trap density (2.148×10^{15} cm^{-3}) but improved mobility (1.857×10^3 $cm^2V^{-1}s^{-1}$) compared to pristine TiO_2. These findings highlight the potential of *meso*-epitaxial TiO_2 for enhancing inorganic perovskite solar cells.

1 | Introduction

Inorganic–organic perovskite (IOP) solar cells have received significant attention recently due to their excellent and promising optoelectronic properties, including long carrier lifespans [1], long diffusion lengths [2], tunable bandgaps [3], and strong light absorption [4]. The lab-scale prototype devices have achieved a power conversion efficiency (PCE) of about 25.5%, rivaling the most reliable technologies available on the market [5]. Despite their exceptional PCEs, IOP-based solar cells are still affected by the slagging knowledge concerning the instability and degradation mechanisms, hindering the next step toward commercialization and real-life application. The hybrid perovskite lattice is highly sensitive to moisture, oxygen, temperature, and continuous illumination, leading to degradation via ion migration, phase segregation, and interfacial reactions. Numerous strategies such as interface engineering, compositional tuning, and encapsulation have been pursued to mitigate these instabilities, yet long-term operational durability remains a critical challenge for IOP-based photovoltaics. Therefore, in-depth knowledge is essential to improve the IOP-based solar cell's performance and stability.

In general, IOP-based solar cells are configured as a sandwich structure with ETL on FTO serving as a photoanode, which is filled with an IOP active layer, capped by a hole transport layer (HTL), and a counter electrode [6]. The ETL is crucial for the extraction of photo-generated electrons at the ETL/perovskite interface and transportation to the electrode. Binary and ternary metal oxides, including tin dioxide (SnO_2) [7], titanium dioxide (TiO_2) [8], zinc–tin oxide (Zn_2SnO_4) [9], niobium oxide (Nb_2O_5) [10], zinc oxide (ZnO) [11], tungsten oxide (WO_3) [12], and aluminum oxide Al_2O_3 [13] are commonly utilized ETLs in perovskite solar cells (PSCs). It is worth noting that SnO_2 and TiO_2 inorganic-ETLs are frequently reported as effective for achieving high-efficiency PSCs [14], due to their favorable optical properties, including transmittance, conduction band alignment, and refractive index [15], as well as their electronic characteristics such as energy structure, trap states, and carrier mobility [16]. Additionally, these materials are recognized for their chemical stability, cost-effectiveness, and ease of nontoxic fabrication. Despite these advantages, SnO_2-based inorganic-hybrid ETLs are prone to chemical instability [17] as a result of oxidizing from Sn^{2+} – Sn^{4+} under exposure to light and ambient conditions [18]. This phenomenon leads to accelerated degradation and consequently compromises the device's stability. Nonetheless, Kim et al. reported PSCs (n-i-p configuration) based on SnO_2 ETL with a champion efficiency of 23.32%, exceeding 21.18% of the TiO_2-based counterpart for the very first time in 2019, despite its disadvantage under UV and aqueous instability [19].

On the other hand, TiO_2 is known for its chemical stability in various applications, including energy storage [20], photocatalysis [21], and photovoltaic technologies [22]. In dye-sensitized solar cells (DSSCs), mesoporous TiO_2 served as an efficient electron transporter, achieving a PCE of 12.3% with liquid electrolytes and porphyrin dyes [23], and reaching up to 15% when employing solid-state hole transporters in conjunction with organometal halide perovskite absorbers [24]. The development of IOP solar cells, which are derived from DSSCs with TiO_2 as ETL [25, 26], have also raved PSCs as one of the most promising solar technologies in recent years [27], due to their chemical stability in aqueous medium [28], low cost, and high PCEs [29]. Nonetheless, TiO_2-based PSCs are still battling their path to commercialization. Factors including intrinsic low bulk electron mobility ($<1\,cm^2V^{-1}s^{-1}$) [30], low conductivity values, severe recombination, interfacial degradation, particularly at the ETL/perovskite interface, issues with reproducibility, challenges associated with large-scale industrial fabrication, and elevated sintering temperatures ($\geq$1000°C) [31], had contributed to suboptimal charge extraction and transport due to poor morphology and controlled thickness of TiO_2 ETL. Therefore, controlling layer thickness and morphology is essential to enhance the quality of TiO_2 ETL in PSCs. Augustine and coworkers used transparent TiO_2 nanoparticles and mesoporous opaque TiO_2 pastes to investigate the effect of thickness and morphology on the ETL for PSCs [32]. Results demonstrated smooth surface morphology and optimal film thickness of transparent TiO_2 to exhibit high transmittance (93%) and conductivity of 4×10^4 S/cm. Additionally, measured PSCs produced low PCEs below 0.38%. This study used ready-made TiO_2 opaque (18NR-AO) and transparent (18NR-T) pastes, expensive materials to produce the ETLs, which results in low photo-electron injection at the ETL/perovskite interface and low device performance. Additionally, poor charge extraction at the interface may be due to increased trap states and low mobility as a result of the low conductivity and improper band alignment with the adjacent $MAPbI_3$ perovskite. These challenges have deprived TiO_2-based PSCs of the opportunity to take a step toward real-life application to this day. Consequently, they have drawn significant attention in the research community, with a high demand for addressing the critical role of TiO_2 charge extraction and transport, and therefore the performance of PSCs toward the Shockley–Queisser limit.

To the best of our knowledge, there are few reports based on FTO/c-TiO_2 and FTO/c-TiO_2/m-TiO_2 thickness and morphology using the spray pyrolysis (SP) technique. Therefore, in this study, we employ the SP technique to optimize the structure, morphology, optical, and electrical properties of FTO/c-TiO_2 and FTO/c-TiO_2/m-TiO_2 thin films. We control the thickness (via deposition time) and morphology to address challenges associated with energy alignment, mobility, trap states, transmittance, electrical conductivity, stability, and low-cost processability for quality perovskite-based photovoltaics.

2 | Experimental

2.1 | Materials

Titanium tetraisopropoxide (TTIP)-99.9%, hydrochloric acid (HCl)-98.9%, ethanol-99.9%, [6,6]-phenyl-C_{70}-butyric acid methyl ester ($PC_{70}BM$)-99%, lead (II) iodide (PbI_2), and cesium iodide (CsI)-99% without additional purity were purchased from Sigma Aldrich.

2.2 | Electron Transport Deposition (TiO_2)

Fluorine-doped tin oxide (FTO) glass substrates were cut into 15 × 15 mm and cleaned by sequential ultrasonication in acetone (15 mL), isopropanol (15 mL), and deionized water (15 mL) for 10 min at 30°C each to remove surface contamination. They were then dried under a nitrogen gas atmosphere. Subsequently, the substrates were placed in a UV-ozone cleaner for 15 min to eliminate residual surface contaminants further and increase wettability. Then, they were positioned on a room-temperature hot plate.

The c-TiO_2 solution (sol) was prepared by gradually adding 7.4 mL of TTIP in 50 mL of ethanol, as demonstrated in Figure 1a. On the other hand, 7.4 mL TTIP and 50 mL HCl were poured into separate 80 mL beakers containing 50 mL of Ethanol. Thereafter, the TTIP + ethanol mixture was subsequently transferred dropwise into the HCL + Ethanol sol to form m-TiO_2 sol as illustrated in Figure 1b. Before deposition, c-TiO_2 sol was stirred at room temperature for 10 min using a magnetic stirrer and transferred to a vertical spray gun suspended 30 cm above the substrates. FTO substrates were preheated gradually to 300°C to avoid staining before spray coating. c-TiO_2 samples were then spray-coated (300 kPa) from 15 to 60 s deposition time, resting 15 s in between to maintain the substrate's temperature at 300°C during each coating interval. Thereafter, samples were allowed to cool to room temperature for an hour, then transferred into a furnace, where annealing was performed at 450°C for an hour in ambient air conditions. Eventually, the films were left in the furnace to cool to room temperature overnight. This procedure was subsequently repeated for the FTO/c-TiO_2/m-TiO_2 thin films as depicted in Figure 1b, with *meso*-treatment at 5, 6, 7, and 10 s deposition time.

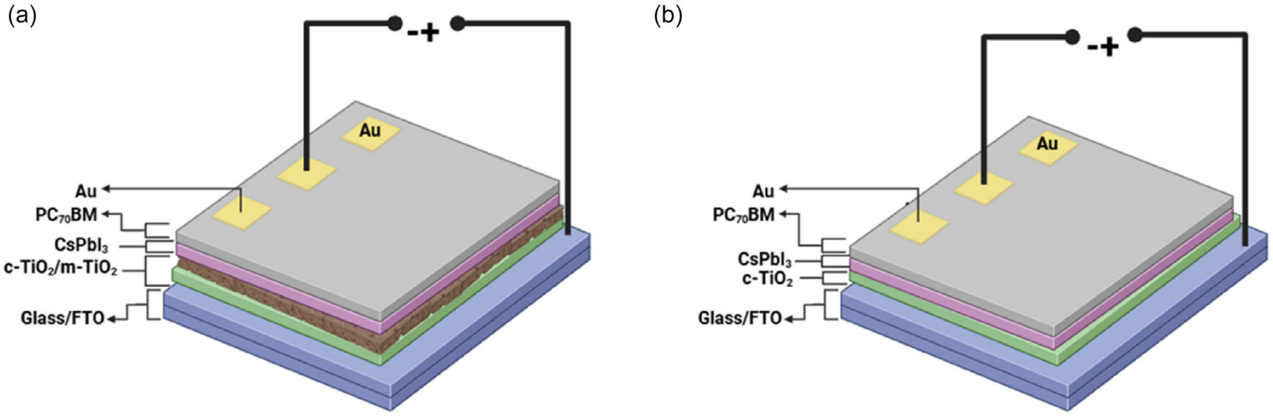

FIGURE 1 | Schematic presentation of electron-only devices (a) without m-TiO$_2$ and (b) with c-TiO$_2$ layer.

2.3 | Electron-Only Device Fabrication

FTO/c-TiO$_2$/ (with/without m-TiO$_2$ layer)/CsPI$_3$/PC$_{70}$BM/Au electron-only devices were fabricated via-SP (TiO$_2$ films) as discussed above and SPVD (CsPbI$_3$ [33]) techniques, as shown in Figure 2a,b, respectively. The ETLs were sprayed on clean glass/FTO and annealed at 450°C. Thereafter, 500 nm CsPbI$_3$ perovskite was deposited using the resistive evaporator Figure 2b and annealed for 30 min, followed by thermal evaporization of 50 nm PC$_{70}$BM and 80 nm gold (Au). Figure 3a and 3b show a schematic presentation of electron-only devices with m-TiO$_2$ and without m-TiO$_2$ layer, respectively. I–V measurements were performed using an Agilent B2912A Source Measure Unit, ORIEL LCS-100 solar simulator with Air-Mass 1.5 Global (AM 1.5 G) filter, and Newport 91150V silicon reference cell for calibration.

2.4 | Film Characterization

The Bruker D2-Phaser X-ray diffraction (XRD) was used to confirm the thin films' structural composition by employing Cu Kα radiation with a wavelength of 1.5405 Å. The angle 2θ between the incident and diffracted rays was varied in steps of 0.05° from 10° to 50°. Properties including structure, crystallinity, crystal size, residual strain, and dislocation density of the films were examined using the diffractogram data. Field emission-scanning electron microscopy (FE-SEM, Zeiss Crossbeam 540) was used to investigate the film's morphology, with the help of ImageJ software, while using the American Standard for Testing and Materials (ASTM). The absorbance and transmittance of the films were measured using a CARY-60 BIO UV–vis spectrometer with incident light wavelengths ranging from 400 to 800 nm. Four-Point Probe (Ossila), equipped with gold plate probes (60 g uniform spring force), was used to measure the sheet resistance and conductivity of FTO/c-TiO$_2$ and FTO/c-TiO$_2$/m-TiO$_2$ inorganic ETL thin films.

3 | Results

3.1 | Structural Properties

The structural properties of c-TiO$_2$ thin films grown and annealed at 450°C without a mesoporous capping layer were analyzed using XRD, as shown in Figure 4a for varying dep times from 15–60 s and Figure 4b for the optimal 45 s deposited film. Annealing at 450°C for 1 h enhanced crystallinity of the rutile TiO$_2$ phase, as confirmed by sharp XRD reflections. 2θ values of 27.4°, 36.1°, and 41.2°, distinct diffraction emerged, corresponding to the (110), (101), and (111) planes, respectively, confirming the rutile phase based on the JCPDS card No. 21–1276. In addition, $a = b = 4.56$ and $c = 7.08$ Å were calculated lattice

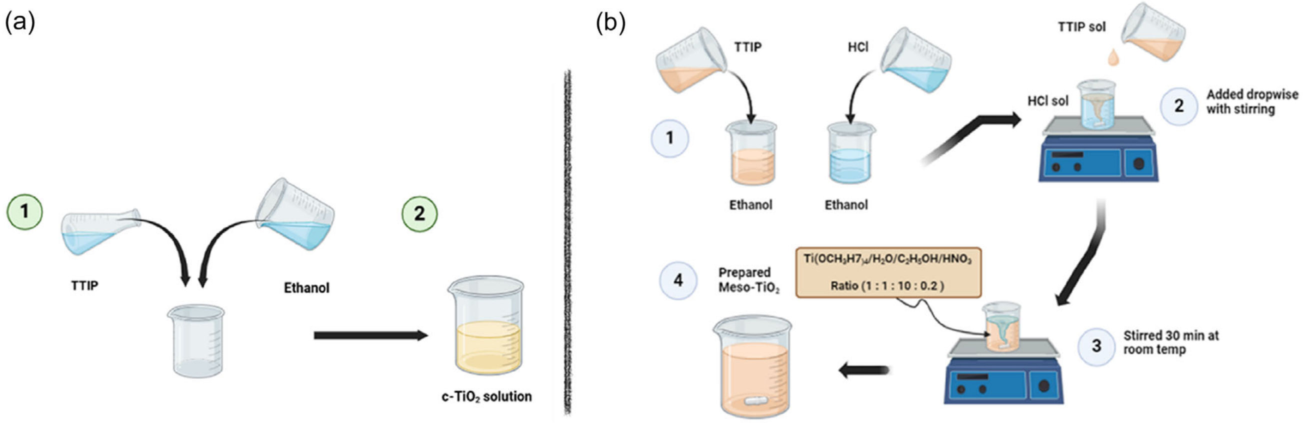

FIGURE 2 | Schematic of synthetic view for (a) c-TiO$_2$ and (b) m-TiO$_2$ solution preparation methods.

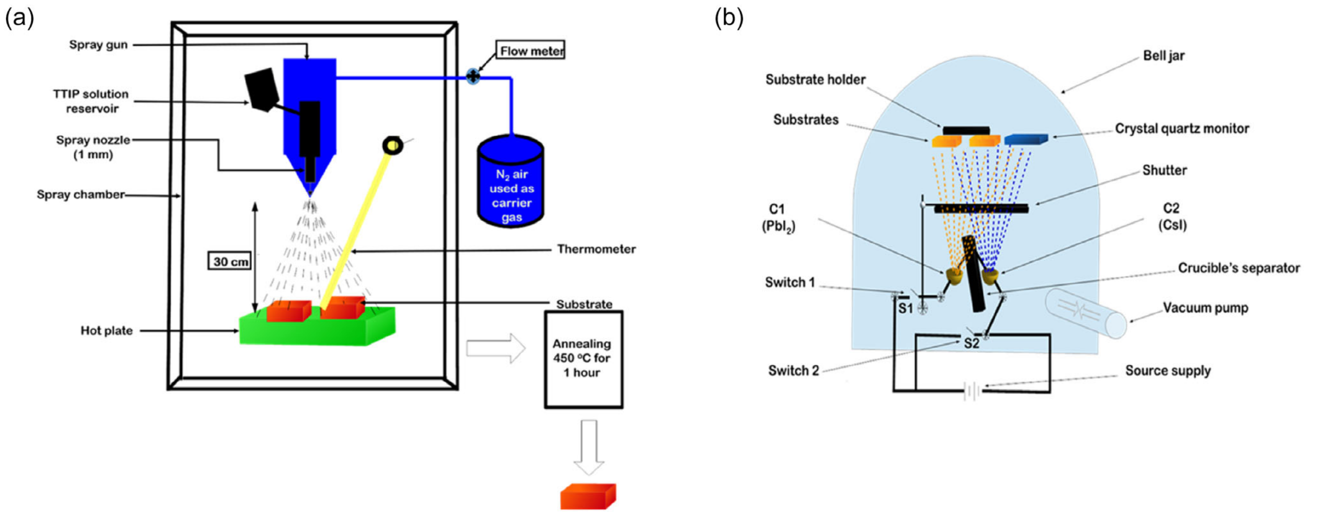

FIGURE 3 | (a) Presentation of SP technique diagram depicting the preparation of FTO/c-TiO_2 and FTO/c-TiO_2/m thin films. (b) Shows the SPVD schematic diagram used to fabricate $CsPbI_3$, $PC_{70}BM$ thin films, and Au back contact.

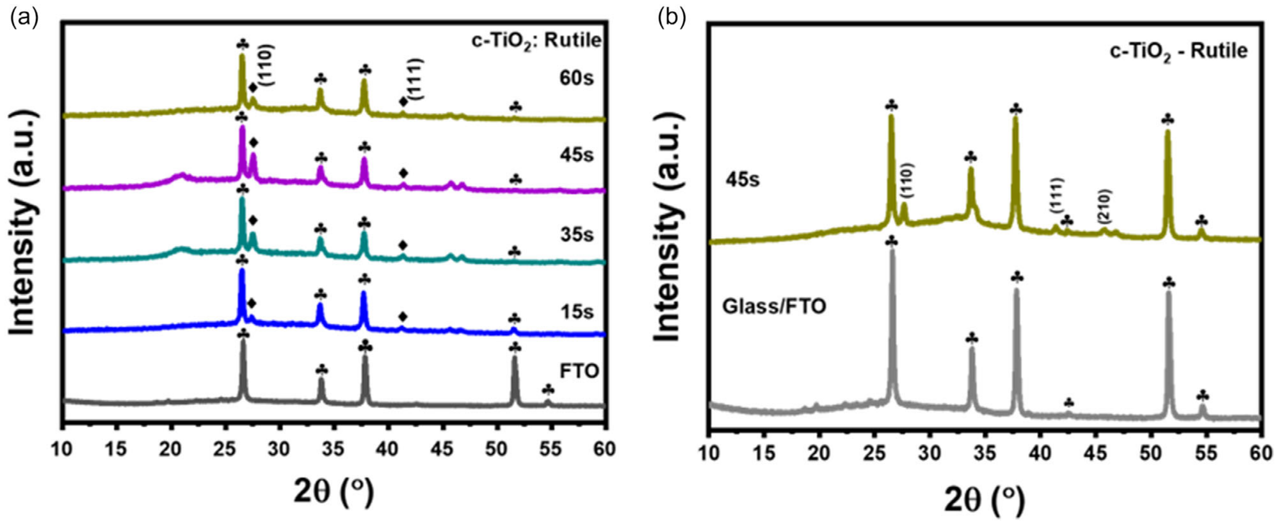

FIGURE 4 | XRD patterns of c-TiO_2 thin films on glass/FTO with (a) varying dep time from 15 to 60 s and (b) the optimal 45 s deposited film.

constants, confirming the tetragonal crystal structure of the films. No evidence of anatase-related peaks was observed, indicating that no phase transition occurred. Moreover, a notable peak increase at 27.4° reveals an increasing trend with deposition time (reaching its optimum at 45 s). According to Ommeaymen et al., the sharp peak is an indication of improved c-TiO_2 film crystallinity and grain growth [34]. Furthermore, such observation may imply that an adequate supply of TiO_2 material is essential for facilitating optimal crystal growth and enhancing atomic diffusion. Wang et al. [25] investigated the lattice mismatch of the rutile (RT) and anatase (AT) phases of TiO_2 films prepared by chemical bath deposition and high-temperature sintering. The RT phase displayed better lattice coordination because of the sharp diffraction peak at 27.4°, proving beneficial for the growth and optimization of c-TiO_2. Two weak peaks were also identified, indicating slight crystallization of the rutile c-TiO_2.

In investigating the optimal thickness of the films deposited in steps of 15 s from 0 to 60 s, as shown in Figure 5a, the calculated crystallite size showed an increase from 22 to 27 nm during 15–60 s. Additionally, the dislocation density calculated using (Equation 1) depicted a decreasing trend from 2.06 to 1.80 nm^{-2} between 15 and 45 s and an increase from 1.80 to 2.61 nm^{-2} between 45 and 60 s, as depicted in Figure 5b. This suggests that the 45 s thickness of the rutile TiO_2 film is optimal, therefore promising to fabricate beneficial ETLs for perovskite-based solar cells.

$$\rho = \frac{n}{D^2} \tag{1}$$

where the dislocation density, denoted as ρ, is related to the crystallite size by the Williamson and Smallman formula, n equals unity for minimum dislocation density.

Stress and strain were examined for the rutile TiO_2 films. Positive slopes depicted in Figure 6a–d demonstrate compressive stress calculated using Equation (2). Compressive strain was observed to reduce with deposition time. Films exhibiting compressive

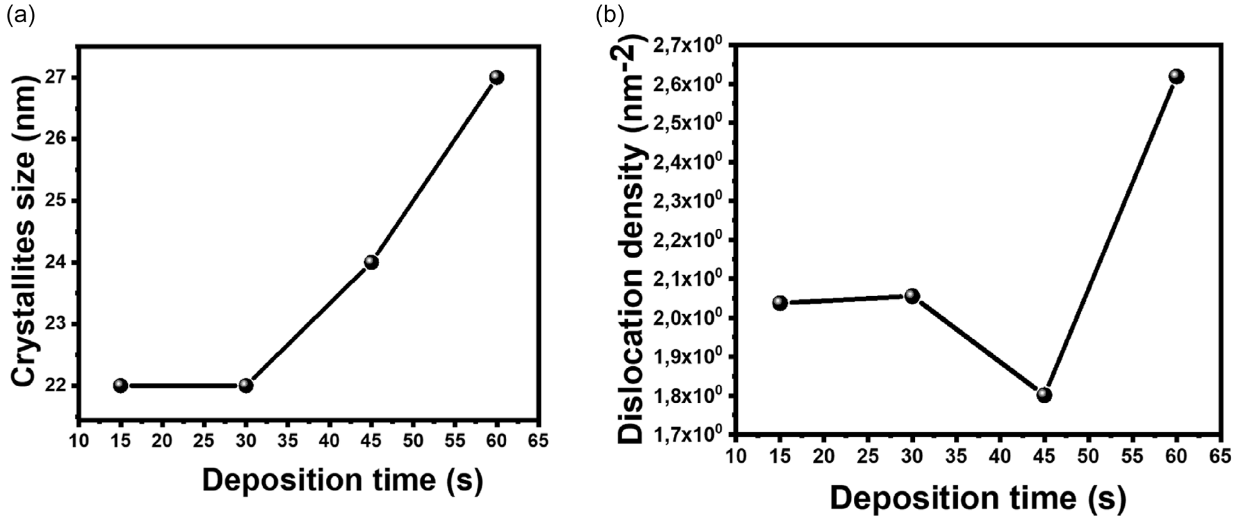

FIGURE 5 | c-TiO_2 thin films with (a) showing crystallite size v/s deposition time and (b) dislocation density v/s deposition time.

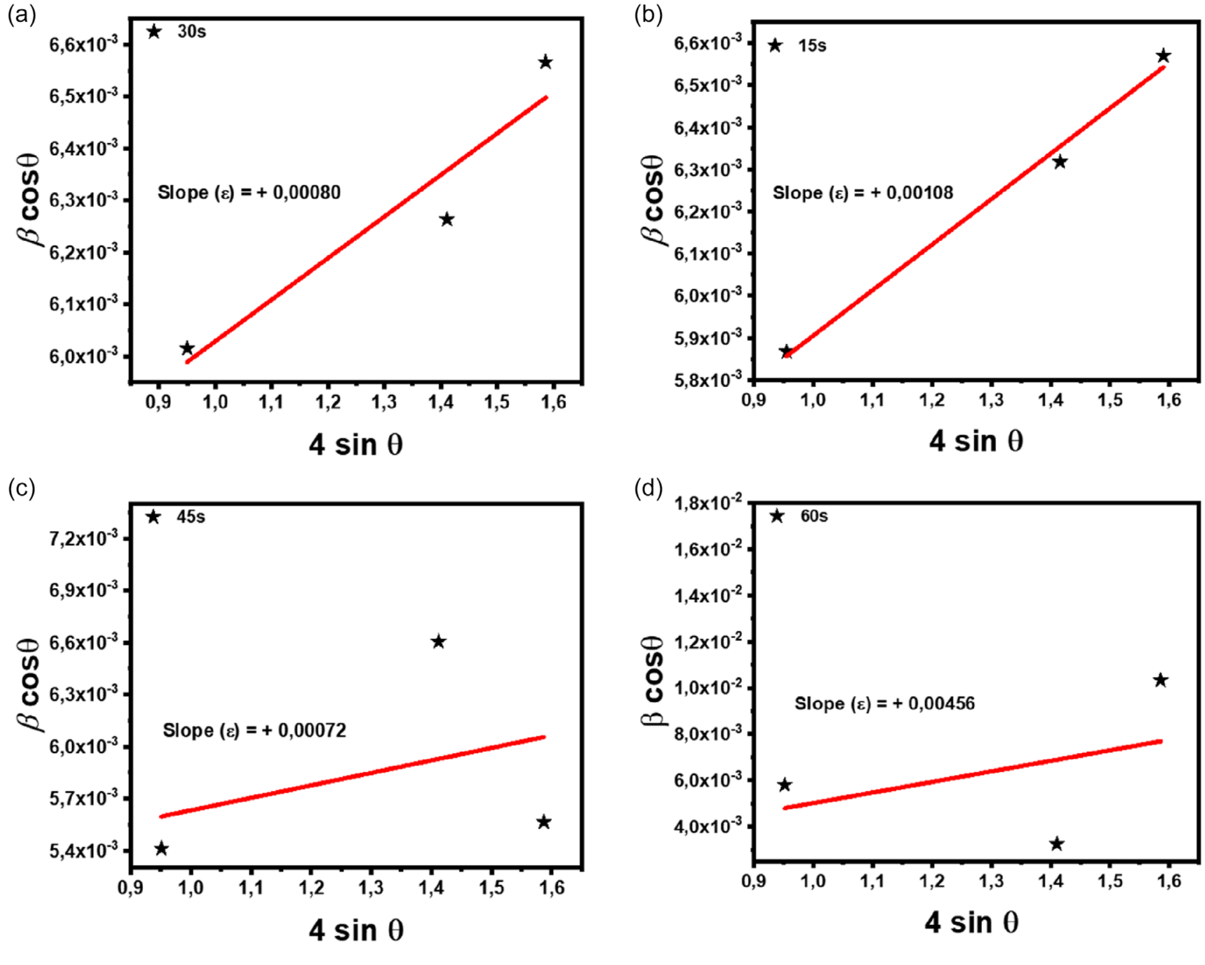

FIGURE 6 | Compressive stress c-TiO_2 (a) 15 s, (b) 30 s, (c) 45 s, and (d) 60 s thin films deposited in steps of 15 s.

strain were investigated by et al. and shown to possess beneficial properties for highly efficient PSCs.

$$\beta \cos \theta = \frac{K\lambda}{D} + 4\varepsilon \sin \theta \tag{2}$$

Moreover, the present study focused on rigid glass/FTO substrates; mechanical properties such as tensile strength and bending stability were not assessed. Since PSCs increasingly target flexible and wearable applications, future work would be to investigate the mechanical robustness of spray-pyrolyzed TiO_2

ETLs on flexible substrates such as PET or ITO, where cracking, adhesion, and bending durability will critically determine device reliability.

3.2 | FESEM

3.2.1 | Surface Morphology Analysis of c-TiO_2 Thin Films

The top-view of FE-SEM images of the c-TiO_2 films prepared by spray pyrolysis technique are shown in Figure 7a–d. Surface morphology was assessed to study the effect of varying deposition time. It is observed in Figure 7a that the film exhibits a relatively uneven surface coverage from a mixture of small and calculated larger grain sizes of about 195.57 nm. Furthermore, the grains appear closely packed. However, unevenly distributed voids make the films susceptible to nonradiative charge carrier recombination. Increasing film thickness improves morphology by reducing defects, enlarging grain size (see the trend in Figure 7e), and enhancing compactness. As shown in Figure 7b, the grains began to coalesce, forming larger aggregates, resulting in a smooth film with an average grain size of about 210.18 nm. In addition, remarkable surface improvement was demonstrated upon increasing the deposition time to 45 s, resulting in a smoother and

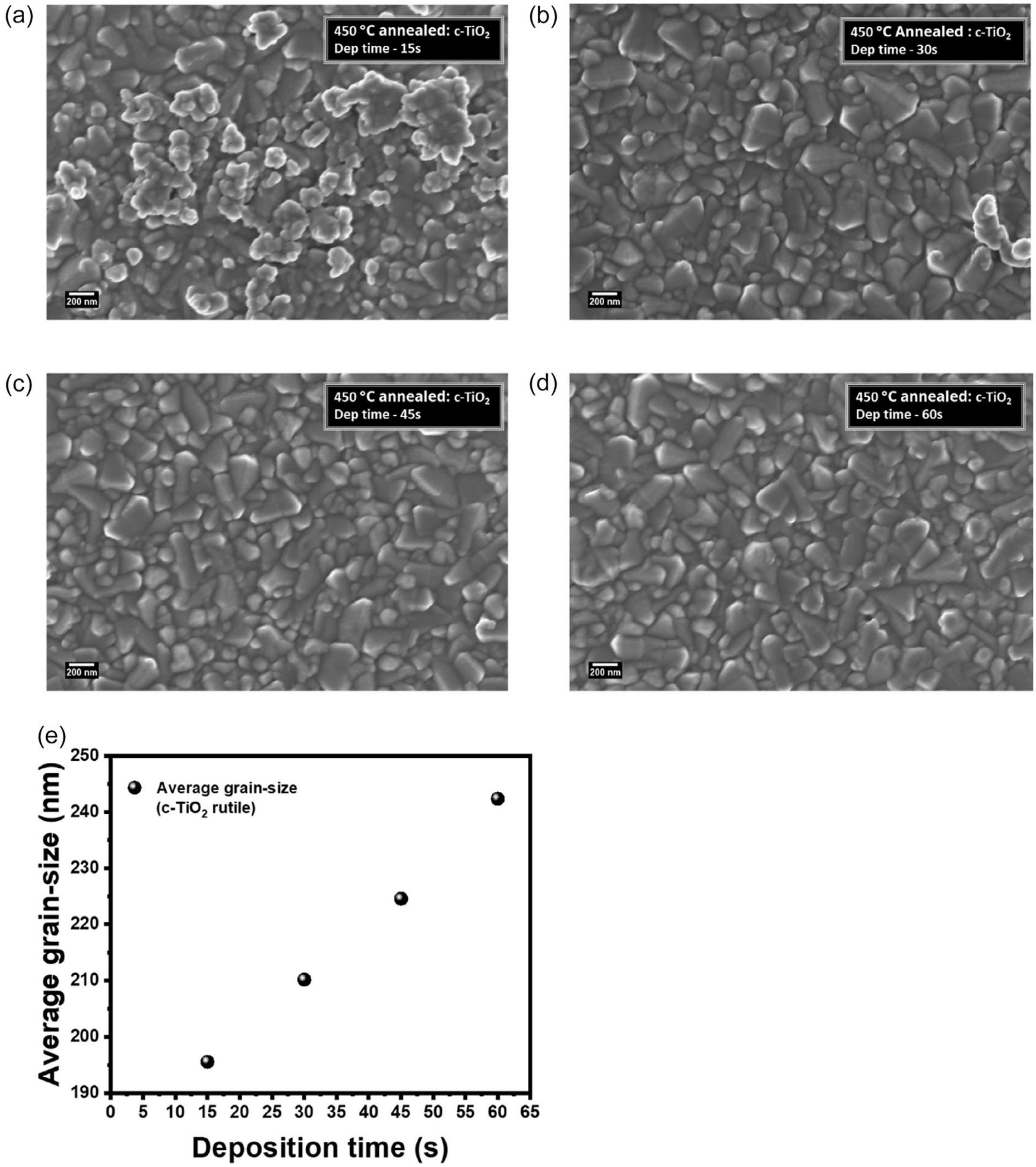

FIGURE 7 | Top-view FE-SEM micrographs depicting the surface morphology of c-TiO_2 thin films at (a) 15 s, (b) 30 s, (c) 45 s, and (d) 60 s deposition times. (e) Displays the effective growth influenced by the increasing average grain size at varying deposition times.

continuous surface, as shown in Figure 7c. The film quality agrees with the demonstrated high crystallinity and low dislocation density as depicted in Figures 4a and 5b, respectively. The estimated average grain size was 224.56 nm, corresponding to the 45 s deposition time of the optimal thickness. Additionally, larger grains depicted in Figure 7d illustrated low defect density as a result of reduced grain boundaries (GBs). However, the excessive thickness (leading to high dislocation density in Figure 5b at 60 s) may introduce mechanical stress resulting from the tensile stress as depicted in Figure 6d. Over time, this leads to instability and the device's performance degradation.

3.2.2 | Surface Morphology Analysis of c-TiO_2 Thin Film Capped with m-TiO_2

The incorporation of m-TiO_2 onto a c-TiO_2 substrate can be observed in the FE-SEM images depicted in Figure 8a–d, which display the morphological evolution of the m-TiO_2 layer at different deposition times (5–10 s), followed by annealing at 450°C. At lower deposition times (5 s), depicted in Figure 8a, the layer appears relatively thin and loosely packed, with smaller spherical particles distributed over the c-TiO_2, which may still be faintly visible in the background, suggesting partial surface coverage. As the deposition time increases from 6 s to 10 s, the mesoporous layer becomes denser, and the particles grow larger and coalesce, indicating enhanced nucleation and growth. The c-TiO_2 layer becomes increasingly obscured and is no longer discernible in the 10 s sample, implying full surface coverage by the m-TiO_2. Pore size within the mesoporous structure appears to increase with deposition time due to the aggregation of particles and formation of larger inter-particle voids. In literature, the pore size of m-TiO_2 has a direct effect on its porous conductivity-larger and more interconnected pores improve electrolyte infiltration and charge transport pathways, enhancing the conductivity of the TiO_2 transport layer. This was observed by Bisquert et al. [35], and O'Regan et al. [36], which highlights that an optimal pore structure significantly enhances electron mobility and reduces recombination losses in dye-sensitized and PSCs.

3.3 | Ultraviolet–Visible Spectroscopy

3.3.1 | Optical Analysis of FTO/c-TiO_2 Thin Film

Figure 9a depicts the UV–vis absorption spectra of c-TiO_2 thin films with varying deposition time for controlled thickness. All films exhibited characteristic c-TiO_2 absorption peaks at 430 and 432 nm, consistent with other reports [37]. Notably, the absorption of the films confirmed improved transparency, with a significant absorption reduction between 380 and 450 nm. This reduction is attributed to the wide bandgap of TiO_2 polymorphs [38], leading to high-quality ETL films in PSCs.

The bandgap (E_g) of the films was estimated using the Tauc's plot equation (Equation (3)) [39], as shown in Figure 9b.

$$\alpha h\nu = C\left(h\nu - E_g\right)^n \tag{3}$$

in this equation, α represents the absorption coefficient, h is Planck's constant, ν denotes the frequency, and C is a constant. E_g corresponds to the bandgap, while n is a constant that

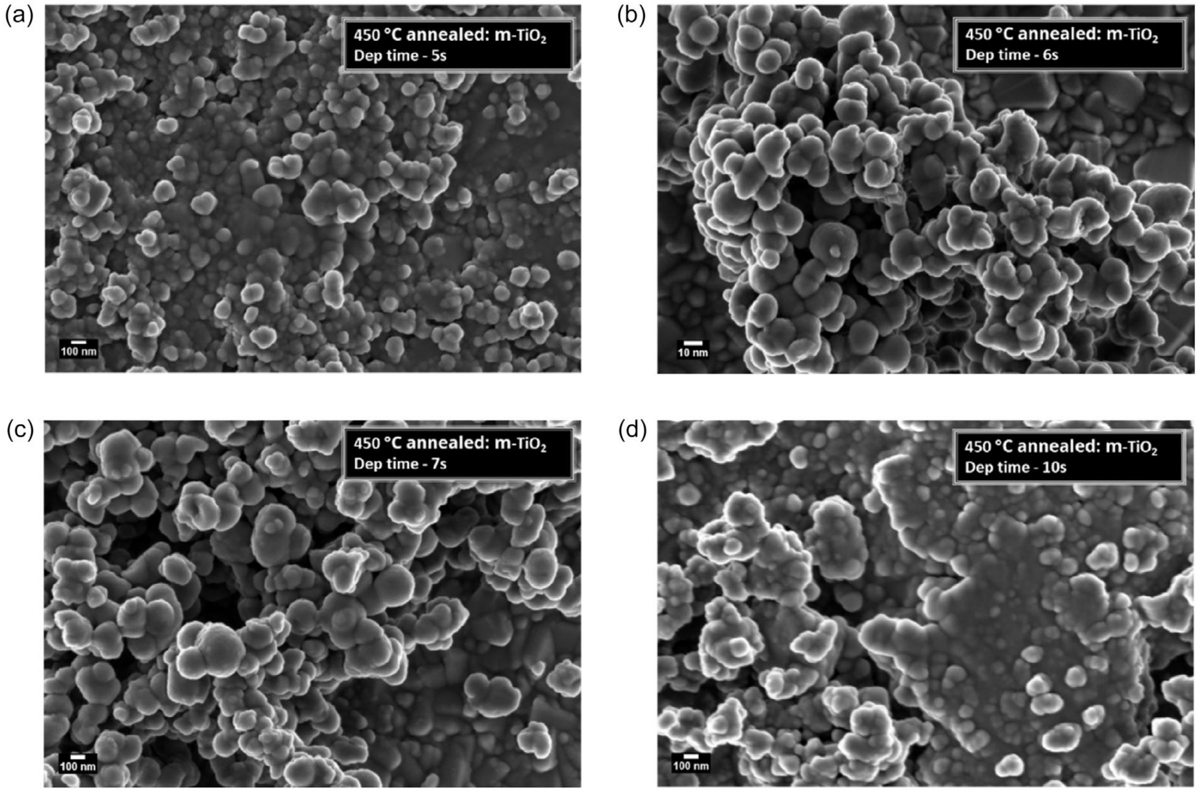

FIGURE 8 | Top-view FE-SEM micrographs depicting an effective grain growth of the rutile m-TiO_2 thin films at (a) 5s, (b) 6s, (c) 7s, and (d) 10s varying deposition times.

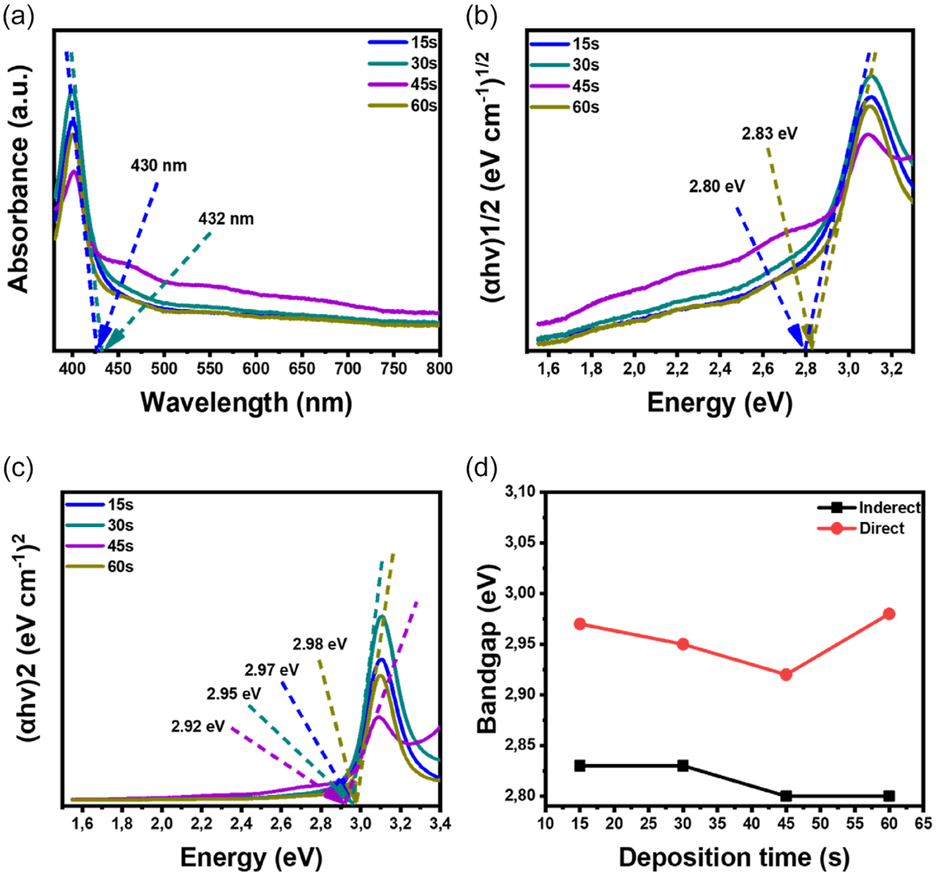

FIGURE 9 | (a) UV-Vis absorption measurements with varying c-TiO_2 deposition time for the band-optical properties of rutile thin films. (b) and (c) Shows estimated band gaps for indirect and direct electronic transition, respectively, estimated using Tauc's plots. (d) Compares the estimated indirect and direct band gaps with varying deposition time for deposited c-TiO_2 thin films using spray pyrolysis.

determines the nature of the electronic transition: $n = 1/2$ for a direct allowed transition (Figure 9b), 2 for an indirect allowed transition (Figure 9c), 3/2 for a direct forbidden transition, and 3 for an indirect forbidden transition.

It was observed that the systematic variation of the deposition time has a marginal effect on the optical bandgap. The direct electronic transition estimated E_g ranging from ≈2.80–2.83 eV, while the indirect transition ranges from ≈2.92–3.0 eV. This indicated that varying the deposition time slightly causes an observed onset redshift, reducing the bandgap of c-TiO_2 films, as shown in Figure 9d, despite its significant impact on absorption intensities. Therefore, this effect may be linked to the increasing grain size reported in Table 1. Gaung-Lei et al. demonstrated the behavior of TiO_2 bandgap reduction with an increase in grain size [40]. Additionally, Jeyakumar et al. demonstrated the thickness and absorption limit of TiO_2 thin films. They achieved a cell efficiency of 29.64%, with Voc, Jsc, and fill factor of 1.241 V, 28.70 mA/cm^2, and 0.83, respectively, with a thickness of 40 nm [41].

3.4 | Photoluminescence

We further examined PL acquisitions to gain deeper insight into the impact of m-TiO_2 on the ETL/perovskite interface. The photoexcitation dynamics (excitation, emission, and recombination) of FTO/c-TiO_2 and FTO/c-TiO_2/m-TiO_2 thin films were analyzed using time-resolved photoluminescence (TRPL). Normalized PL emission spectra of the pristine and *meso*-incorporated TiO_2 thin films are shown in Figure 10a. The emission intensity increased upon m-TiO_2 incorporation, with m-TiO_2: 7 s resulting in ≈2.7–3-fold lesser increment, indicating a reduction in radiative recombination with increasing deposition time. Figure 10b shows both normalized absorption and PL emission spectra of the pristine and optimal samples. It can be observed that the PL emission for the optimized FTO/c-TiO_2 with m-TiO_2: 7 s deposited film is higher than the pristine, suggesting a film with improved carrier charge transport. Additionally, their onset emission peak at 400 nm corresponds with the onset absorption peaks at 430–432 nm. This further confirms that the incorporation of

TABLE 1 | Average grain size for FTO/c-TiO_2 and FTO/c-TiO_2/m-TiO_2 thin films grown using a spray pyrolysis technique at varying deposition times.

Deposition time(s)	FTO/c-TiO_2 (nm)	Deposition time(s)	FTO/c-TiO_2/m-TiO_2(nm)
c-TiO_2: 15	195.57	m-TiO_2: 5s	77.41
c-TiO_2: 30	210.18	m-TiO_2: 6s	14.63
c-TiO_2: 45	224.56	m-TiO_2: 7s	15.74
c-TiO_2: 60	242.34	m-TiO_2: 10s	109.68

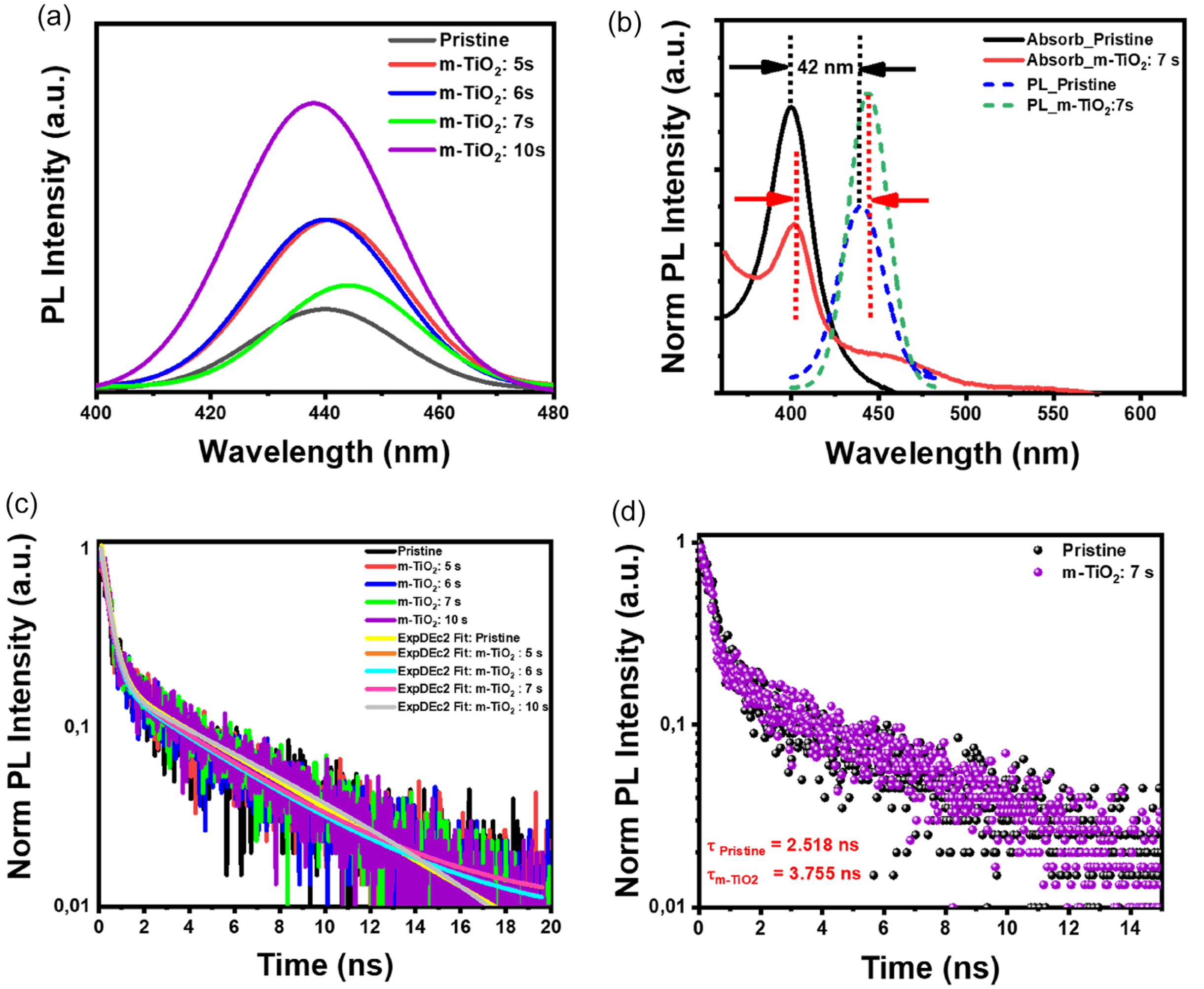

FIGURE 10 | Normalized (a) mission spectra of pristine and *meso*-incorporated, (b) absorbance and PL emission peaks of TiO_2 thin films, with the (c) lifetime biexponential fitted decaying curves. (d) Comparison of the pristine and *meso*-incorporated TiO_2 lifetime decay curves.

the m-TiO_2 layer does not affect the bandgap of the c-TiO_2 film. However, further analysis demonstrated that the pristine and *meso*-incorporated TiO_2 thin films exhibit a relatively small Stokes' shift of ≈42 nm. This redshift could be due to the strong electron–phonon coupling in its lattice, leading to energy loss during the relaxation process [42]. Consequently, this suggests that the PL emission characteristics are likely to be associated with the direct exciton recombination process.

Figure 10c shows the TRPL lifetime decay measurements of pristine and m-TiO_2 ETL thin films. The decay curves were fitted using a biexponential decay function illustrated in (Equation 4). The fitted parameters are presented in Table 2, where the average charge carrier recombination lifetimes were determined using (Equation 5).

$$J(t) = C_1^{\left(-\frac{y}{\tau 1}\right)} + C_1^{\left(-\frac{y}{\tau 1}\right)} \qquad (4)$$

$$\langle \tau \rangle = (C_1\tau_1^2 + C_2\tau_2^2)/(C_1\tau_1 + C_2\tau_2) \qquad (5)$$

where τ_1 and τ_2 denote the fast and slow decay components, corresponding to surface trapping and radiative recombination, respectively. C_1 and C_2 represent the decay amplitudes. The pristine TiO_2 depicted in Figure 10d exhibited a fast decay lifetime of 0.2652 ns and a slow decay lifetime of 3.4022 ns, resulting in an average lifetime of 2.510 ns. In contrast, the optimized FTO/c-TiO_2 with m-TiO_2: 7 s deposited film exhibited a fast decay lifetime of 0.2267 ns and a slow decay lifetime of 4.768 ns with the corresponding average lifetime of 3755 ns. The average lifetime increased by a factor of 0.67, while the slow decay lifetime increased by a factor of 0.71. This suggests a reduction in trap-assisted recombination as a result of incorporating the m-TiO_2 layer.

TABLE 2 | TiO_2 thin films analyzed as a function of varying m-TiO_2 layer, with PL fitted parameters.

Deposition time (s)	C_1	τ_1 (ns)	C_2	τ_2 (ns)	τ_{avg} (ns)
Pristine	0.9292	0.2652	0.1845	3.4022	2.510
m-TiO_2: 5 s	0.9292	0.2651	0.1845	3.3989	2.513
m-TiO_2: 6 s	1.0404	0.2488	0.1798	3.4691	2.525
m-TiO_2: 7 s	1.0997	0.2267	0.1823	4.7668	3.755
m-TiO_2: 10 s	1.2249	0.2517	0.1921	4.0897	3.008

3.5 | Electrical Measurements

Electrical conductivity measurements were conducted using an FPP-EM system to understand the effect of m-TiO_2 on the c-TiO_2 thin films, as shown in Figure 11a. The sheet resistance and conductivity were measured for FTO/c-TiO_2 and FTO/c-TiO_2/m-TiO_2 thin films. It is observed that conductivity increases from 3.18×10^6 to 7.21×10^7 S/m, inversely proportional to the reduction of the sheet resistivity from 7.34 to 6.33 Ω/□, upon introduction of m-TiO_2 at 5–10 s deposition time. This could be attributed to the larger mesopores as a result of the smaller grains depicted in Figure 8a. Wang et al., confirmed that m-TiO_2 pore characteristics are inversely proportional to the grain size [43]. In contrast, conductivity was observed to increase rapidly from 7.21×10^4 to 9.52×10^6 S/m, achieving optimal conductivity at m-TiO_2: 7 s film thickness. It is worth noting that Takahashi et al. [44], linked this behavior to improved interconnection within the TiO_2 film and confirmed adequate surface coverage from the small grains, which can be observed in Table 1. The conductivity enhancement observed upon annealing (450°C) may be attributed to improved crystallite connectivity and possible generation of oxygen vacancies, which are known to act as shallow donors in rutile TiO_2.

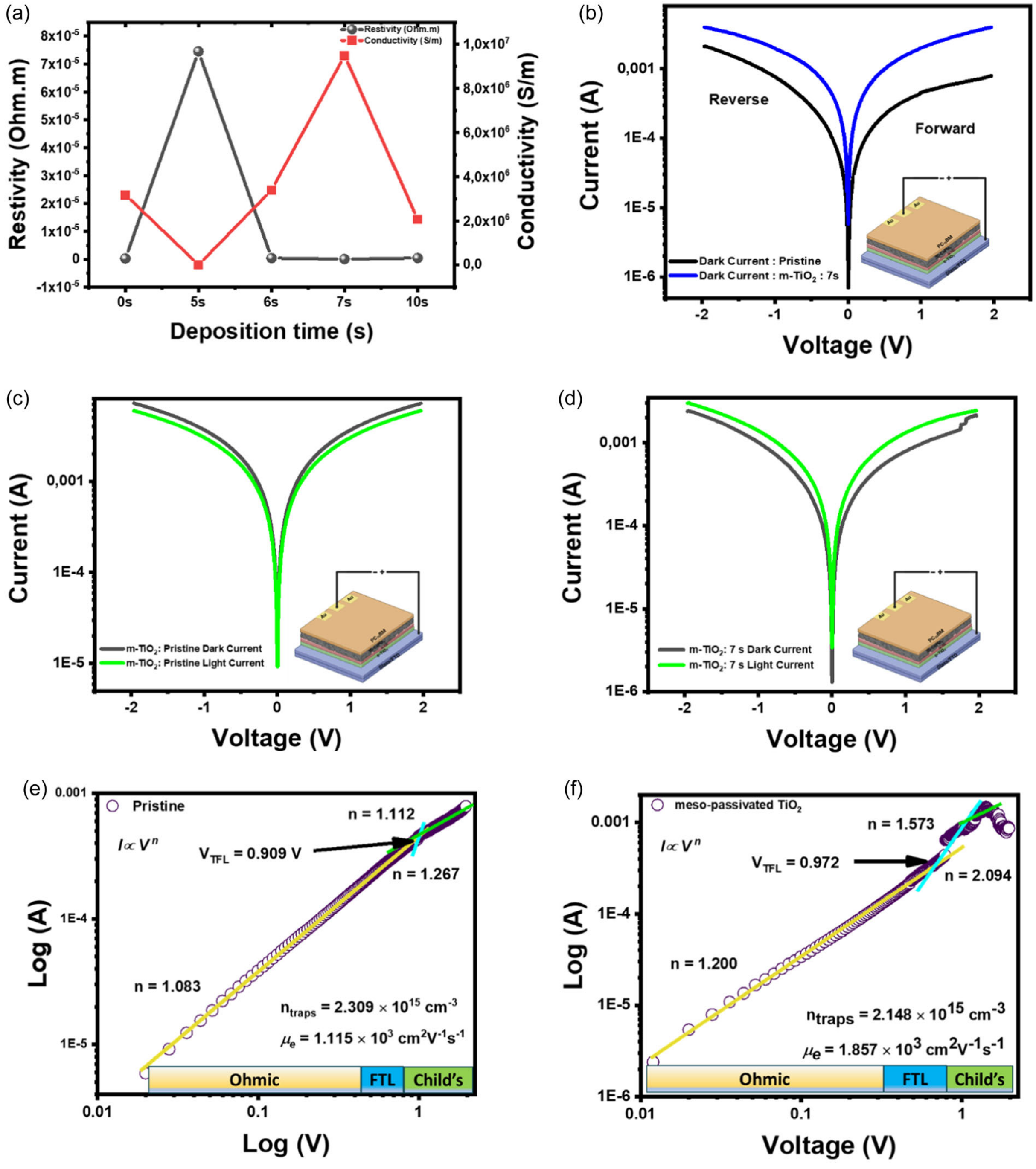

FIGURE 11 | Device analyses, including (a) electrical conductivity plot versus dep time and (b) a schematic illustration of the device architecture. Plots in (c) and (d) display electrical semilog for dark current, with (d) comparing dark and light current of FTO/c-TiO_2/m-TiO_2/$CsPbI_3$/$PC_{70}BM$/Au devices. Lastly, (e) and (f) show log–log transport analysis for electron mobility and density of trap states.

Although Raman spectroscopy is often used to probe such effects, our XRD and electrical analyses already provide a consistent indication that the films remain rutile and that any defect formation enhances rather than degrades transport properties

We further investigated the effect of the m-TiO_2 layer on the electrical properties of the resulting films. Figure 11b depicts semi-logarithmic I–V curves of pristine and m-TiO_2 optimal under dark current analysis. It can be observed that the generated dark current is higher upon incorporation of m-TiO_2, further confirming the role played in improving the ETL/perovskite interface, charge collection, and charge transport. Figure 11c,d show semi-log I–V curves of the pristine and m-TiO_2-treated devices, respectively, under dark and illumination (AM 1.5G, 100 mW·cm^{-2}) conditions. Notably, all curves exhibit symmetry around 0 V. Furthermore, the current measured under illumination exceeds the dark current in the m-TiO_2-treated device, confirming the generation of charge carriers upon exposure to light. On the contrary, the pristine device shows a lesser light response, this may be attributed to the degree of dislocation density displayed in Figure 5b. Additionally, this could also be associated with the large structural tensile stress observed from the microstrain slope in Figure 5d of the XRD measurements.

To measure the density of trap states on pristine and m-TiO_2-treated thin films, we employed space charge limited current (SCLC) as depicted in Figure 11e,f, respectively. The double-log I–V characteristics of the electron-only device, shown in Figure 11e,f, revealed that the onset voltage of the trap-filled limit region (V_{TFL}) decreased from 0.909 to 0.892 V upon m-TiO_2 treatment. According to Equations (6) and (7), the corresponding diode ideality factor (η) decreases from 2.5 to 1.6, signifying suppressed trap-assisted recombination and a shift toward more ideal diode behavior. These observations indicate that m-TiO_2 interlayer mitigates electronic defects, thereby improving charge-carrier transport and reducing nonradiative losses in the device.

$$I = I_s\left(e^{\frac{q}{\eta kT}} - 1\right) \tag{6}$$

and

$$\eta = \frac{q}{mkT} \tag{7}$$

where I and I_s are defined as the diode current and reverse saturated current, respectively, q is the electric charge (1.602×10^{-19} C), V is the voltage applied, k is Boltzmann's constant (1.381×10^{-23}J/K), T is absolute temperature (298.15 K), m is the slope of the $ln(I)$ versus V plot, and η is the ideality factor.

Furthermore, the trap state defect density (N_t) in TiO_2 thin films (with and without m-TiO_2 treatment) was calculated using the Mott–Gurney Law (Equation 8) based on dark I–V measurements of the electron-only device [45].

$$V_{\mathrm{TFL}} = \frac{eN_tL^2}{2\varepsilon_0\varepsilon} \tag{8}$$

where, ε_0 is the free space permittivity, ε is the dielectric constant (5.8) of the $CsPbI_3$ around the 435 nm absorption edge [46], L is the thickness of $CsPbI_3$, and V_{TFL} is the trap-filled limit region onset voltage. The treatment of c-TiO_2 films with m-TiO_2 resulted in a decrease in defect density from 2.309×10^{15} to 2.148×10^{15} cm^{-3}, which can be attributed to the interfacial band energy alignment and enhanced film quality. It is observed that charge carrier mobility increased from 1.115×10^3 to 2.148×10^3 cm^{2}V^{-1}s^{-1} with the reduction of trap states. This phenomenon correlates with the PL lifetime measurements, where m-TiO_2-treated films exhibited a longer charge carrier lifetime. The charge carrier mobility (μ) values were calculated using (Equation 9).

$$J = \frac{9}{8}\mu\varepsilon_0\varepsilon\frac{V^2}{L^3} \tag{9}$$

where μ is the electron mobility, V is the voltage, and J is the current density.

Accordingly, we report the values extracted from SCLC as apparent mobilities (μSCLC) and note that the 1.93 increase (from 1.115×10^3 to 2.148×10^3 cm^{2}V^{-1}s^{-1}) for m-TiO_2 treated devices reflects a combination of: (1) reduced trap density and improved charge extraction at the ETL/perovskite interface, (2) improved film microstructure and intergrain connectivity, and (3) measurement artifacts intrinsic to SCLC in ionic/soft semiconductors (e.g., VTFL shifts due to mobile ions, contact resistance effects, or uncertainty in ε and L). To validate these trends, we therefore recommend more independent mobility measurements, including Hall effect (van-der-Pauw), time of flight (TOF), transient terahertz or microwave conductivity (TRMC/THz).

4 | Conclusion

In this study, the ETL configuration comprising an FTO/c-TiO_2 layer capped with an m-TiO_2 layer was systematically optimized using a spray pyrolysis technique. By carefully controlling the deposition time, significant enhancements were observed in the films' structural, morphological, optical, and electrical properties.

These improvements in ETL quality directly translated to enhanced device performance. The increased conductivity and reduced recombination losses are critical factors in achieving higher short-circuit current densities (Jsc) and fill factors (FF), while the improved carrier lifetime supports a higher open-circuit voltage (Voc) due to suppressed trap-assisted recombination. Compared to literature values, the performance metrics of our optimized architecture are competitive with those of vapor-deposited or chemically engineered ETLs depicted in Table 3. For example, Yin et al. [49] and Wang et al. [48] achieved similar improvements using mesoporous layers; however, their approaches often involved additional processing steps or costly fabrication techniques. In contrast, our method provides a cost-effective and scalable strategy that maintains performance parity. Moreover, the enhanced compactness and surface coverage of the ETL contribute to better environmental stability by acting as a barrier to moisture and ion migration, factors that are particularly relevant for the phase stability of all-inorganic perovskites like $CsPbI_3$. Overall, the ETL optimization presented here not only boosts charge extraction efficiency but also contributes to the

TABLE 3 | Comparison of TiO_2-based ETL properties, highlighting mobility and trap density improvements. Demonstration of the competitive performance (structurally, morphologically, optically, and electronically) of the optimized FTO/c-TiO_2/m-TiO_2 film, highlighting the benefits of the SP method and interfacial engineering.

Study	ETL Structure	Fabrication Method	Crystallite Size (nm)	Conductivity (S/m)	Sheet Resistance (Ω/□)	Carrier Lifetime (ns)	Trap Density N_t (cm^{-3})	Mobility μ ($cm^2V^{-1}s^{-1}$)	Notes
Thisstudy	FTO/c-TiO_2/ m-TiO_2	Spray pyrolysis	22–24	3×10^6 $\rightarrow 1.18 \times 10^7$	7.4 → 6.33	2.510 → 3.755	2.31×10^{15} $\rightarrow 2.15 \times 10^{15}$	1.12×10^3 $\rightarrow 2.15 \times 10^3$	Optimized at 45s (c-TiO_2) + 7s (m-TiO_2); improved grain coalescence and PL response
Liu et al. [47],	FTO/c-TiO_2	Spin coating	≈18	$\approx 1 \times 10^6$	≈8	≈3.2	$\approx 4 \times 10^{15}$	$\approx 1 \times 10^3$	Good stability; single-layer ETL
Wang et al. [48],	FTO/c-TiO_2	Atomic layer deposition	≈7.5	$\approx 1.3 \times 10^6$	≈7.5	≈3.5	$\approx 3–5 \times 10^{15}$	$\approx 0.9–1.2 \times 10^3$	Good morphology control, expensive
Yin et al.	FTO/c-TiO_2/ m-TiO_2	Spray pyrolysis	≈6.5	$\approx 7 \times 10^6$	≈6.5	≈3.4	$\approx 2.8 \times 10^{15}$	$\approx 1.3 \times 10^3$	Improved infiltration and defects
Zhang et al. [49],	FTO/TiO_2	Vacuum deposited	22–22	$\approx 9 \times 10^6$	≈6.7	≈3.6	$\approx 2.5 \times 10^{15}$	$\approx 1.5 \times 10^3$	Compatible with full processing

longevity and reliability of $CsPbI_3$-based PSCs, underscoring the significance of interfacial engineering in advancing perovskite photovoltaic technology.

In terms of industrial viability, spray pyrolysis presents clear advantages for large-area perovskite photovoltaics. The technique is scalable to roll-to-roll or sheet-based manufacturing and can uniformly coat substrates well beyond laboratory dimensions with minimal material wastage. Compared with high-cost methods such as atomic layer deposition (ALD) or vacuum deposition, SP requires lower capital investment and operational expenses, thereby reducing the overall cost per unit area. These attributes position FTO/c-TiO_2/m-TiO_2 ETLs prepared by SP as a promising pathway for industrial-scale $CsPbI_3$ PSC fabrication, bridging the gap between laboratory optimization and commercial deployment.

Acknowledgments

The authors wish to thank the University of Pretoria and NRF-South Africa, grant no. N01156/115463 of the SARChI for financial support. The authors also acknowledge Prof. R Erasmus (WITS) for the PL acquisitions.

Funding

This work was supported by the University of Pretoria and the NRF-South Africa (Grant: N01156/115463).

Conflicts of Interest

The authors declare no conflicts of interest.

Data Availability Statement

The data that support the findings of this study are available from the corresponding author upon reasonable request.

References

1. A. Urbina, “The Balance between Efficiency, Stability and Environmental Impacts in Perovskite Solar Cells: A Review,” *Journal of Physics: Energy* 2, no. 2 (2020): 022001.

2. T. Das, N. K. Rana, and A. Guchhait, “Structural Optimization of Inverted CsPbI2Br Perovskite Solar Cells for Enhanced Performance via SCAPS-1D Simulation,” *Physica Scripta* 98, no. 7 (2023): 075928.

3. Y. Wang, M. Zhang, K. Xiao, et al., “Recent Progress in Developing Efficient Monolithic All-Perovskite Tandem Solar Cells,” *Journal of Semiconductors* 41, no. 5 (2020): 051201.

4. H. Lu, X. Guo, C. Yang, and S. Li, “*Tailoring perovskite compounds for broadband light absorption*,” in IOP Conference Series: Materials Science and Engineering, (IOP Publishing, 2018).

5. N. Skandalos, V.. Kapsalis T. Ma, and D. Karamanis, “Towards 30% Efficiency by 2030 of Eco-Designed Building Integrated Photovoltaics,” *Solar* 3, no. 3 (2023): 434–457.

6. D. Zhou, T. Zhou, Y. Tian X. Zhu, and Y. Tu, “Perovskite-Based Solar Cells: Materials, Methods, and Future Perspectives,” *Journal of Nanomaterials* 2018, no. 1 (2018): 8148072.

7. K. Deng, Q. Chen, and L. Li, “Modification Engineering in SnO_2 Electron Transport Layer toward Perovskite Solar Cells: Efficiency and Stability,” *Advanced Functional Materials* 30, no. 46 (2020): 2004209.

8. M. M. Tavakoli, P. Yadav, R. Tavakoli, and J. Kong, “Surface Engineering of TiO_2 ETL for Highly Efficient and Hysteresis-less Planar Perovskite Solar Cell (21.4%) with Enhanced Open-Circuit Voltage and Stability,” *Advanced Energy Materials* 8, no. 23 (2018): 1800794.

9. R. K. Poobalan, R. Ramanathan, R. Chellakumar, K. Ravichandran, and M. Zinigrad, “Enhancing the Perovskite Solar Cell Performance by the Interface Modification of Zn–Sn–O Compound Heterostructures,” *Materials Advances* 4, no. 24 (2023): 6704–6717.

10. A. Hosen, M. S. Mian, and S. R. A. Ahmed, “Improving the Performance of Lead-Free FASnI3-Based Perovskite Solar Cell with $NbO_{52}O_5$ as an Electron Transport Layer,” *Advanced Theory and Simulations* 6, no. 2 (2023): 2200652.

11. A. Kumar, U. Gupta, R. Chaujar, M. Tripathi, and N. Gupta, “Simulation of Perovskite Solar Cell Employing ZnO as Electron Transport Layer (ETL) for Improved Efficiency,” *Materials Today: Proceedings* 46 (2021): 1684–1687.

12. Y. You, W. Tian, L. Min, F. Cao, K. Deng, and L. Li, “TiO_2/WO_3 Bilayer as Electron Transport Layer for Efficient Planar Perovskite Solar Cell with Efficiency Exceeding 20%,” *Advanced Materials Interfaces* 7, no. 1 (2020): 1901406.

13. J. Dagar, S. Castro-Hermosa, G. Lucarelli, A. Zampetti, F. Cacialli, and T. M. Brown, “Low-Temperature Solution-Processed Thin SnO_2/Al_2O_3 Double Electron Transport Layers toward 20% Efficient Perovskite Solar Cells,” *IEEE Journal of Photovoltaics* 9, no. 5 (2019): 1309–1315.

14. J. Zhang, J. Fu, Q. Chen, et al., “3, 5-Difluorophenylboronic acid-modified SnO_2 as ETLs for perovskite solar cells: PCE> 22.3%, T82> 3000 h,” *Chemical Engineering Journal* 433 (2022): 133744.

15. S. Lettieri, M. Pavone, A. Fioravanti, L. S. Amato, and P. Maddalena, “Charge Carrier Processes and Optical Properties in TiO_2 and TiO_2-Based Heterojunction Photocatalysts: A Review,” *Materials* 14, no. 7 (2021): 1645.

16. T. Sewela, R. Ocaya, and T. Malevu, “Recent Insights into the Transformative Role of Graphene-Based/TiO_2 Electron Transport Layers for Perovskite Solar Cells,” *Energy Science & Engineering* 13, no. 1 (2025): 4–26.

17. S. Yadav, S. Kumari, S. K. Ghoshal, R. Kumar, S. K. Chaudhary, and D. Mohan, “Effect of Ultraviolet Radiation Exposure on Optical Nonlinearity and Switching Traits of SnO_2 Thin Films Deposited by Thermal Evaporation,” *Optics & Laser Technology* 133 (2021): 106575.

18. A. Iatsenko, A. Mishchenko, and B. Kornilovych, “Investigation of Thermal Stability, Optical Properties, Phase and Chemical Composition of Transparent Conductive Tin Oxide Films Deposited by Pyrolytic Method on Silica Float Glass.,” *Technology Audit and Production Reserves* 5, no. 3 (2019): 10–14.

19. M. Kim, J.. Jeong, H. Lu, et al., “Conformal Quantum Dot–SnO_2 Layers as Electron Transporters for Efficient Perovskite Solar Cells,” *Science* 375, no. 6578 (2022): 302–306.

20. P. Si, Z.. Zheng, Y. Gu, et al., “Nanostructured TiO_2 Arrays for Energy Storage,” *Materials* 16, no. 10 (2023): 3864.

21. S. Peiris, H. B. de Silva, K. N. Ranasinghe, S. V. Bandara, and I. R. Perera, “Recent Development and Future Prospects of TiO_2 Photocatalysis,” *Journal of the Chinese Chemical Society* 68, no. 5 (2021): 738–769.

22. Z. Barlow, Z. Wei, and R. Wang, “Boosting Lithium Polysulfide Conversion via TiO_2-Supported Niobium Catalyst for Lithium Sulfur Battery,” *Materials Chemistry and Physics* 314 (2024): 128830.

23. A. Yella, H.-W. Lee, H. N. Tsao, et al., “*Porphyrin-Sensitized Solar Cells with Cobalt (II/III)–based Redox Electrolyte Exceed 12% Efficiency. Science*, 334, no. 6056 (2011): 629–634.

24. H.-S. Kim, C.-R. Lee, J.-H. Im, et al., “Lead Iodide Perovskite Sensitized All-Solid-State Submicron Thin Film Mesoscopic Solar Cell with Efficiency Exceeding 9%,” *Scientific Reports* 2, no. 1 (2012): 591.

25. Z. Dong, H. Ren, C. M. Hessel, et al., “Quintuple-Shelled SnO_2 Hollow Microspheres with Superior Light Scattering for High-Performance Dye-Sensitized Solar Cells.,” *Advanced Materials* 26, no. 6 (2013): 905–909.

26. P.-Y. Su, J.-M. Liu, X.-L. Lin, et al., “Multichromophoric Di-Anchoring Sensitizers Incorporating a Ruthenium Complex and an Organic Triphenyl Amine Dye for Efficient Dye-Sensitized Solar Cells,” *Inorganic Chemistry Frontiers* 2, no. 11 (2015): 1040–1044.

27. D. Yang, R. Yang, S. Priya, and S. Liu, “Recent Advances in Flexible Perovskite Solar Cells: Fabrication and Applications,” *Angewandte Chemie International Edition* 58, no. 14 (2019): 4466–4483.

28. J.-M. Herrmann, H. Tahiri, Y. Ait-Ichou, G. Lassaletta, A. Gonzalez–Elipe, and A. Fernandez, “Characterization and Photocatalytic Activity in Aqueous Medium of TiO2 and Ag-TiO_2 Coatings on Quartz,” *Applied Catalysis B: Environmental* 13, no. 3-4 (1997): 219–228.

29. S. Yun, X. Zhou, J. Even, and A. Hagfeldt, “Theoretical Treatment of $CH_3NH_3PbI_3$ Perovskite Solar Cells,” *Angewandte Chemie International Edition* 56, no. 50 (2017): 15806–15817.

30. A. Raj, M. Kumar, A. Kumar, et al., “Effect of Doping Engineering in TiO_2 Electron Transport Layer on Photovoltaic Performance of Perovskite Solar Cells,” *Materials Letters* 313 (2022): 131692.

31. S. Marinel, D.H. Choi, R. Heuguet, D. Agrawal, and M. Lanagan, “Broadband Dielectric Characterization of TiO_2 Ceramics Sintered through Microwave and Conventional Processes,” *Ceramics International* 39, no. 1 (2013): 299–306.

32. D. Augustine, E.S. Rosa, N. Prastomo, and S. Shobih, “Optimization of Titanium Dioxide Nanoparticles in Mesoporous Electron Transport Layer Perovskite Solar Cell,” *Jurnal Elektronika Dan Telekomunikasi* 20, no. 1 (2020): 23–28.

33. S. Sibiya and M. Diale, “Growth and Characterization of Orthorhombic Cesium Lead Tri-Iodide Perovskite Thin-Films by Sequential Physical Vapor Deposition for Solar Cells,” *Materials Science and Engineering: B* 322 (2025): 118673.

34. O. Sheikhnejad-Bishe, F. Zhao, A. Rajabtabar-Darvishi, E. Khodadad, A. Mostofizadeh, and Y. Huang, “Performance of TiO_2 Nanoparticles,” *International Journal of Electrochemical Science* 9, no. 8 (2014): 4230–4240.

35. J. Bisquert, “Chemical Diffusion Coefficient of Electrons in Nanostructured Semiconductor Electrodes and Dye-Sensitized Solar Cells,” *The Journal of Physical Chemistry B* 108, no. 7 (2004): 2323–2332.

36. B. O’regan and M. Grätzel, “*A Low-Cost, High-Efficiency Solar Cell Based on Dye-Sensitized Colloidal TiO_2 Films. Nature*, 353, no. 6346 (1991): 737–740.

37. A. Sadeghzadeh-Attar and M. R. Bafandeh, “Effect of Annealing on UV-Visible Absorption and Photoluminescence Behavior of Liquid Phase Deposited TiO_2 Nanorods,” *International Journal of Applied Ceramic Technology* 16, no. 6 (2019): 2429–2440.

38. F. Z. Haque, R. Nandanwar, and P. Singh, “Evaluating Photodegradation Properties of Anatase and Rutile TiO_2 Nanoparticles for Organic Compounds,” *Optik* 128 (2017): 191–200.

39. E. Davis and N. Mott, “Conduction in Non-Crystalline Systems V. Conductivity, Optical Absorption and Photoconductivity in Amorphous Semiconductors,” *Philosophical Magazine* 22, no. 179 (1970): 0903–0922.

40. T. Guang-Lei, H. Hong-Bo, and S. Jian-Da, “Effect of Microstructure of TiO_2 Thin Films on Optical Band Gap Energy, *Chinese Physics Letters* 22, no. 7 (2005): 1787.

41. R. Jeyakumar, A. Bag, R. Nekovei, and R. Radhakrishnan, “Influence of Electron Transport Layer (TiO_2) Thickness and Its Doping Density on the Performance of $CH_3NH_3PbI_3$-Based Planar Perovskite Solar Cells,” *Journal of Electronic Materials* 49, no. 6 (2020): 3533–3539.

42. D. B. Straus, S. Hurtado Parra, N. Iotov, et al., “Direct Observation of Electron–phonon Coupling and Slow Vibrational Relaxation in Organic–inorganic Hybrid Perovskites,” *Journal of the American Chemical Society* 138, no. 42 (2016): 13798–13801.

43. X. Wang, Y. Yao, W. Gao, and Z. Zhan, “High-Rate and High Conductivity Mesoporous TiO_2 Nano Hollow Spheres: Synergetic Effect of Structure and Oxygen Vacancies,” *Ceramics International* 47 (2021): 13572–13581.

44. S. Takahashi, S. Uchida, P.V. Jayaweera, S. Kaneko, and H. Segawa, “Impact of Compact TiO_2 Interface Modification on the Crystallinity of Perovskite Solar Cells,” *Scientific Reports* 13, no. 1 (2023): 16068.

45. D. Yang, R. Yang, K. Wang, et al., “High Efficiency Planar-Type Perovskite Solar Cells with Negligible Hysteresis Using EDTA-Complexed SnO_2,” *Nature Communications* 9, no. 1 (2018): 3239.

46. R. K. Singh, R. Kumar, N. Jain, S. R. Dash, J. Singh, and A. Srivastava, “Investigation of Optical and Dielectric Properties of $CsPbI_3$ Inorganic Lead Iodide Perovskite Thin Film,” *Journal of the Taiwan Institute of Chemical Engineers* 96 (2019): 538–542.

47. C. Liu, H. Su, C. Wei, et al., “Tunable Electronic Properties of TiO_2 Nanocrystals by in Situ Dopamine Functionalization for Planar Perovskite Solar Cells,” *Electrochimica Acta* 354 (2020): 136720.

48. J. Wang, Z. Dong, J. Wang, et al., “Room-Temperature Processed TiO_2 to Construct Composite Electron Transport Layers for Efficient Planar Perovskite Solar Cells,” *Journal of Materials Chemistry A* 11, no. 41 (2023): 22206–22215.

49. X. Zhang, Y. Zhang, Y. Wang, et al., “Improving the Performance of Perovskite Solar Cells via TiO_2 Electron Transport Layer Prepared by Direct Current Pulsed Magnetron Sputtering,” *Journal of Alloys and Compounds* 929 (2022): 167278.

Supporting Information

Additional supporting information can be found online in the Supporting Information section. **Supporting Fig. S1:** Grain size distribution histograms of m-TiO_2 films deposited at different times. The histograms show the frequency of grain sizes obtained from FE-SEM image analysis (via ImageJ) for deposition times of (a) 15 s, (b) 30 s, (c) 45 s, and (d) 60 s. The data indicate a shift toward larger grain sizes with increasing deposition time, consistent with agglomeration and coalescence of nanoparticles. Error bars represent the statistical variation in grain sizes extracted from multiple regions of each sample. **Supporting Fig. S2:** V–Vis transmittance spectra of c+m-TiO_2 films deposited for 5, 6, 7, and 10 s. The spectra show a strong absorption edge below ≈380 nm, corresponding to the TiO_2 bandgap region, followed by increased transmittance in the visible range. The sample deposited for 7 s exhibits the highest transmittance (≈80%) in the 400–600 nm region, suggesting reduced light scattering and improved film uniformity at this deposition time, whereas films deposited for shorter (5–6 s) or longer (10 s) times show lower transmittance, likely due to incomplete coverage or agglomeration effects.